



A Journal of the Gesellschaft Deutscher Chemiker

# Angewandte Chemie

GDCh

International Edition

www.angewandte.org

## Accepted Article

**Title:** Construction of Hierarchical Hollow Co<sub>9</sub>S<sub>8</sub>/ZnIn<sub>2</sub>S<sub>4</sub> Tubular Heterostructures for Highly Efficient Solar Energy Conversion and Environmental Remediation

**Authors:** Gu-Ping Zhang, Dong-Yun Chen, Na-Jun Li, Qing-Feng Xu, Hua Li, Jing-Hui He, and Jian-Mei Lu

This manuscript has been accepted after peer review and appears as an Accepted Article online prior to editing, proofing, and formal publication of the final Version of Record (VoR). This work is currently citable by using the Digital Object Identifier (DOI) given below. The VoR will be published online in Early View as soon as possible and may be different to this Accepted Article as a result of editing. Readers should obtain the VoR from the journal website shown below when it is published to ensure accuracy of information. The authors are responsible for the content of this Accepted Article.

**To be cited as:** *Angew. Chem. Int. Ed.* 10.1002/anie.202000503  
*Angew. Chem.* 10.1002/ange.202000503

**Link to VoR:** <http://dx.doi.org/10.1002/anie.202000503>  
<http://dx.doi.org/10.1002/ange.202000503>

# Construction of Hierarchical Hollow $\text{Co}_9\text{S}_8/\text{ZnIn}_2\text{S}_4$ Tubular Heterostructures for Highly Efficient Solar Energy Conversion and Environmental Remediation

Guping Zhang, Dongyun Chen, Najun Li, Qingfeng Xu, Hua Li, Jinghui He, and Jianmei Lu\*

**Abstract:** The rational construction of heterojunctions and design of photocatalyst structures are considered effective approaches to enhance photocatalytic activities. Herein, visible-light-responsive hierarchical  $\text{Co}_9\text{S}_8/\text{ZnIn}_2\text{S}_4$  tubular heterostructures are fabricated by growing two-dimensional  $\text{ZnIn}_2\text{S}_4$  nanosheets on one-dimensional hollow  $\text{Co}_9\text{S}_8$  nanotubes. This rational design combines two photoresponsive sulfide semiconductors in a stable heterojunction with a hierarchical hollow tubular structure, improving visible-light absorption, yielding a large surface area, exposing sufficient catalytically active sites, and effectively promoting the separation and migration of photogenerated charges. The as-prepared hierarchical  $\text{Co}_9\text{S}_8/\text{ZnIn}_2\text{S}_4$  nanotubes thus exhibit excellent photocatalytic  $\text{H}_2$  evolution and Cr(VI) reduction efficiency. Under visible-light illumination, the optimized  $\text{Co}_9\text{S}_8/\text{ZnIn}_2\text{S}_4$  heterostructure provides a remarkable  $\text{H}_2$  generation rate of  $9039 \mu\text{mol h}^{-1} \text{g}^{-1}$  without the use of any co-catalysts (metal complex, noble metal, etc.), and Cr(VI) is completely reduced in 45 min. The  $\text{Co}_9\text{S}_8/\text{ZnIn}_2\text{S}_4$  heterostructure also displays long-term stability after multiple photocatalytic cycles. Finally, the relevant photogenerated charge-transfer and catalytic mechanisms of the  $\text{Co}_9\text{S}_8/\text{ZnIn}_2\text{S}_4$  heterostructures are proposed and analyzed.

## Introduction

The widespread use of semiconductor photocatalysts and clean solar energy is considered an effective strategy to address current environmental and energy crises.<sup>[1]</sup> Traditional semiconductor metal oxides such as stannic oxide ( $\text{SnO}_2$ ), ceric dioxide ( $\text{CeO}_2$ ), zinc oxide ( $\text{ZnO}$ ), and titanium dioxide ( $\text{TiO}_2$ ) are wide-band-gap photocatalysts and only absorb ultraviolet (UV) light, which greatly limits their photocatalytic efficiency and practical applications.<sup>[2]</sup> Today, because of their excellent optical absorption properties, suitable band gaps, and unique electronic structure, numerous metal sulfides are attracting considerable research attention as visible-light-response catalysts for environmental purification and solar energy conversion.<sup>[3]</sup>

Among the diverse metal sulfide photocatalysts currently being investigated,  $\text{ZnIn}_2\text{S}_4$ , as a ternary chalcogenide semiconductor, is widely recognized as a promising photocatalyst because of its suitable band gap (2.2–2.6 eV),

tunable morphological structure, and strong visible-light absorption.<sup>[4]</sup> In addition, two-dimensional (2D)  $\text{ZnIn}_2\text{S}_4$  nanosheets can offer high surface areas and rich catalytically active sites, which is beneficial for participation in various photocatalytic redox reactions (e.g., photocatalytic  $\text{H}_2$  evolution, Cr(VI) reduction, and  $\text{CO}_2$  conversion).<sup>[5]</sup> However, the photocatalytic performance of pure  $\text{ZnIn}_2\text{S}_4$  remains unsatisfactory, mainly because of the rapid recombination rate of the photogenerated electrons ( $e^-$ ) and holes ( $h^+$ ).<sup>[6]</sup> Multiple previous studies have shown that the construction of a heterojunction with another appropriate metal sulfide semiconductor is an effective approach to enhance photoabsorption and improve the photocatalytic activity of  $\text{ZnIn}_2\text{S}_4$  photocatalysts.<sup>[4b, 5a, 7]</sup>

As a noble-metal-free cobalt sulfide photocatalyst,  $\text{Co}_9\text{S}_8$  has many advantages including its narrow band gap (0.9–1.4 eV), high conduction-band position, and efficient charge transfer.<sup>[4b, 8]</sup> Thus,  $\text{Co}_9\text{S}_8$  has recently begun to attract attention as a potential co-catalyst and is gradually being used in the treatment of environmental pollution and energy conversion. For example, Tan and co-workers coupled 0D  $\text{Co}_9\text{S}_8$  nanoparticles with hierarchical flower-like CdS to produce a composite that significantly improved photocatalytic  $\text{H}_2$  evolution.<sup>[9]</sup> In addition, Gu and colleagues prepared a  $\text{Co}_9\text{S}_8/\text{g-C}_3\text{N}_4$  composite photocatalyst using a simple hydrothermal method for simultaneous Cr(VI) reduction and 2,4-dichlorophenoxyacetic acid (2,4-D) oxidation.<sup>[10]</sup> These findings indicate the potential of  $\text{Co}_9\text{S}_8$  as a co-catalyst with  $\text{ZnIn}_2\text{S}_4$  to not only improve the capacity of visible-light absorption but also promote the separation of photogenerated electrons ( $e^-$ ) and holes ( $h^+$ ), which will eventually enhance the photocatalytic activity.

In addition, advanced morphologic structure design is also necessary to further enhance the photocatalytic performance of semiconductors. Materials with hollow structures have attracted widespread attention as photocatalysts for environmental and energy-related applications because of the following advantages: (1) Hollow structure materials possess high specific surface areas with more reactive sites to participate in the photocatalytic redox reactions. (2) Light reflection and scattering caused by hollow structures contribute to enhanced solar-light absorption and utilization efficiency. (3) The thin-shelled topologies can be beneficial for shortening the transmission distance of charge carriers. (4) The rapid mass transfer in open hollow structures can accelerate reaction progress. In addition, growing 2D semiconductor nanosheets on hollow materials to form hierarchical hollow structures can expose more accessible catalytically active sites and increase the electrolyte–photocatalyst contact area compared with that of simple hollow structures.<sup>[11]</sup>

Based on the above considerations, we report the fabrication of hierarchical  $\text{Co}_9\text{S}_8/\text{ZnIn}_2\text{S}_4$  tubular heterostructures (**Scheme 1**) by growing 2D  $\text{ZnIn}_2\text{S}_4$  nanosheets on the surface of 1D hollow  $\text{Co}_9\text{S}_8$  nanotubes for enhanced visible-light  $\text{H}_2$  evolution

[a] G.P. Zhang, Prof. D.Y. Chen, Prof. N.J. Li, Prof. Q.F. Xu, Prof. H. Li, Prof. J.H. He, and Prof. J.M. Lu, College of Chemistry, Chemical Engineering and Materials Science Collaborative Innovation Center of Suzhou Nano Science and Technology, Soochow University, Suzhou 215123 (P. R. China)

lujm@suda.edu.cn

Supporting information for this article is given via a link at the end of the document.

and reduction of aqueous Cr(VI). This unique design of a hierarchical hollow tubular structure not only provides a larger surface area and abundant reaction sites in the photocatalytic reactions but also ensures full contact of visible-light-active  $\text{ZnIn}_2\text{S}_4$  and  $\text{Co}_9\text{S}_8$ , which can effectively facilitate the separation and transfer of photogenerated electrons and holes. For these reasons, the optimized  $\text{Co}_9\text{S}_8/\text{ZnIn}_2\text{S}_4$  heterostructure displays the highest photocatalytic activity, and the reduction efficiency of Cr(VI) reaches up to 100% within 45 min. In addition, the prepared  $\text{Co}_9\text{S}_8/\text{ZnIn}_2\text{S}_4$  photocatalyst affords an outstanding  $\text{H}_2$  evolution rate of  $9039 \mu\text{mol h}^{-1} \text{g}^{-1}$  without the use of co-catalysts; this rate is 11.2 times higher than that of pure  $\text{ZnIn}_2\text{S}_4$ . Finally, the corresponding catalytic mechanism for  $\text{Co}_9\text{S}_8/\text{ZnIn}_2\text{S}_4$  heterostructures in this study was proposed and analyzed.



**Scheme 1.** Schematic illustration of the fabrication process of hierarchical  $\text{Co}_9\text{S}_8/\text{ZnIn}_2\text{S}_4$  tubular photocatalyst.

## Results and Discussion

The morphology of the as-prepared  $\text{Co}_9\text{S}_8$  nanotubes was first examined using SEM and TEM. **Figure 1a** presents an SEM image of the precursor  $\text{Co}(\text{CO}_3)_{0.35}\text{Cl}_{0.20}(\text{OH})_{1.10}$  nanorod bunches, which had widths of 100–300 nm and lengths of several micrometers. In addition, the XRD pattern of the prepared precursor (**Figure S1a**) shows that all the diffraction peaks were consistent with the standard card of  $\text{Co}(\text{CO}_3)_{0.35}\text{Cl}_{0.20}(\text{OH})_{1.10}$  (JCPDS No. 38-547).<sup>[12]</sup> **Figure 1b** and **c** display SEM and TEM images of the obtained  $\text{Co}_9\text{S}_8$  nanotubes after treating the precursor at 160 °C in  $\text{Na}_2\text{S}$  solution, which clearly reveals their hollow structures. Consistent with the XRD analysis (**Figure S1b**), the two sets of distinct lattice fringes with spacings of 0.281 and 0.296 nm correspond to the (222) and (311) planes of  $\text{Co}_9\text{S}_8$ , respectively (**Figure 1d**).<sup>[4b, 7, 8a]</sup> Furthermore, the corresponding EDX spectrum (**Figure S2a**) and elemental mapping (**Figure 1e**) confirm that the  $\text{Co}_9\text{S}_8$  nanotubes with hollow feature consisted of Co and S elements.

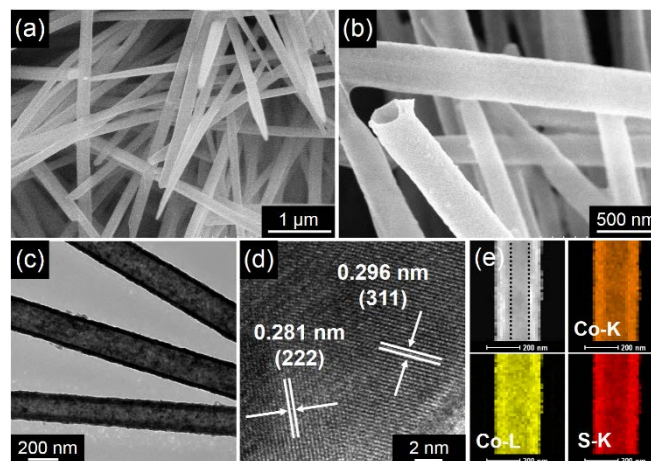


**Figure 1.** SEM images of (a) as-prepared  $\text{Co}(\text{CO}_3)_{0.35}\text{Cl}_{0.20}(\text{OH})_{1.10}$  nanorod bunches and (b)  $\text{Co}_9\text{S}_8$  nanotubes. (c) TEM and corresponding (d) HRTEM images of the  $\text{Co}_9\text{S}_8$  nanotubes. (e) HAADF-STEM and EDX elemental mapping images of Co and S of the  $\text{Co}_9\text{S}_8$  nanotube.

Subsequently, ultrathin  $\text{ZnIn}_2\text{S}_4$  nanosheets were grown on the surface of  $\text{Co}_9\text{S}_8$  nanotubes in a low-temperature solvothermal process. The morphology and structure of the  $\text{Co}_9\text{S}_8/\text{ZnIn}_2\text{S}_4$  composite were characterized using SEM, TEM, and high-resolution TEM (HRTEM) using the 10%- $\text{Co}_9\text{S}_8/\text{ZnIn}_2\text{S}_4$  composite as the model. As illustrated in **Figure 2a**, the  $\text{ZnIn}_2\text{S}_4$  ultrathin nanosheets were uniformly and densely coated on the surface of  $\text{Co}_9\text{S}_8$  nanotubes, forming  $\text{Co}_9\text{S}_8/\text{ZnIn}_2\text{S}_4$  hierarchical tubular heterostructures. Representative TEM images of the 10%- $\text{Co}_9\text{S}_8/\text{ZnIn}_2\text{S}_4$  composite are displayed in **Figure 2b** and **c**. It is apparent that the entire surface of the 1D  $\text{Co}_9\text{S}_8$  nanotubes with open ends was homogeneously covered with  $\text{ZnIn}_2\text{S}_4$  nanosheets, further indicating that the  $\text{Co}_9\text{S}_8/\text{ZnIn}_2\text{S}_4$  composite possessed a hierarchical hollow core–shell configuration. The heterojunction between the layered  $\text{ZnIn}_2\text{S}_4$  nanosheets and  $\text{Co}_9\text{S}_8$  nanotubes is shown in the HRTEM images in **Figure S3**. The lattice spacing is 0.322 nm, which corresponds to the (102) planes of  $\text{ZnIn}_2\text{S}_4$ .<sup>[5b]</sup> In addition, the lattice fringes with a relative low contrast and a lattice spacing of 0.281 nm correspond to the (222) crystal plane of  $\text{Co}_9\text{S}_8$ . The EDX spectrum (**Figure S2b**) and elemental mappings (**Figure 4d**) of a single  $\text{Co}_9\text{S}_8/\text{ZnIn}_2\text{S}_4$  nanotube suggest the homogeneous distribution of Co, S, Zn, and In in the composite. For comparison, the flower-like  $\text{ZnIn}_2\text{S}_4$  spheres were also finally prepared under similar conditions without  $\text{Co}_9\text{S}_8$  nanotubes as a substrate (**Figure S4**). It is known that the larger specific surface area is favorable to photocatalytic activity owing to provide more active sites and efficient transport paths for reactants and products in photocatalytic reactions.<sup>[9]</sup> Nitrogen adsorption–desorption isotherm experiments were therefore performed and the results were shown in **Figure S5**. The nitrogen adsorption-desorption isotherms of pure  $\text{ZnIn}_2\text{S}_4$  and 10%- $\text{Co}_9\text{S}_8/\text{ZnIn}_2\text{S}_4$  composite exhibited type IV isotherm with an obvious hysteresis loop (H3 type) in the higher relative pressure ( $P/P_0 = 0.4\text{--}1.0$ ) range, suggesting the existence of mesopores within the materials.<sup>[4a, 5c, 9]</sup> Using their plots, the BET surface areas of  $\text{ZnIn}_2\text{S}_4$  and 10%- $\text{Co}_9\text{S}_8/\text{ZnIn}_2\text{S}_4$  were

calculated, and the 10%-Co<sub>9</sub>S<sub>8</sub>/ZnIn<sub>2</sub>S<sub>4</sub> composite showed an enhanced Brunauer–Emmett–Teller (BET) surface area (104.32 m<sup>2</sup> g<sup>-1</sup>) in comparison with pure ZnIn<sub>2</sub>S<sub>4</sub> (50.91 m<sup>2</sup> g<sup>-1</sup>). This means that uniformly loading of ZnIn<sub>2</sub>S<sub>4</sub> nanosheets can effectively increase the specific surface area of the composite, which could provide more active sites of the photocatalytic reaction. Simultaneously, the corresponding pore size distribution curve indicate the existence of mesopores in 10%-Co<sub>9</sub>S<sub>8</sub>/ZnIn<sub>2</sub>S<sub>4</sub> composite (Figure S6), which will facilitate the mass transfer for heterogeneous catalysis.<sup>[4b]</sup>

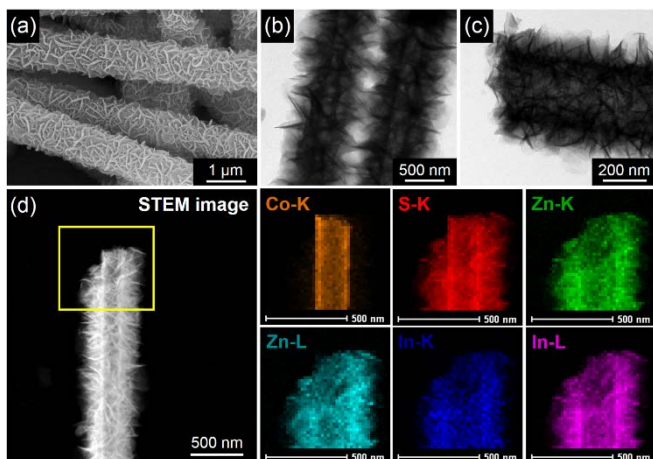


**Figure 2.** (a) SEM and (b–c) TEM images of the prepared 10%-Co<sub>9</sub>S<sub>8</sub>/ZnIn<sub>2</sub>S<sub>4</sub> composite. (d) HAADF-STEM and EDX elemental mapping images of Co, S, Zn, and In of the 10%-Co<sub>9</sub>S<sub>8</sub>/ZnIn<sub>2</sub>S<sub>4</sub> composite.

X-ray diffraction (XRD) was used to characterize the phase composition and crystal structure of the as-prepared Co<sub>9</sub>S<sub>8</sub>, ZnIn<sub>2</sub>S<sub>4</sub>, and Co<sub>9</sub>S<sub>8</sub>/ZnIn<sub>2</sub>S<sub>4</sub> samples. As shown in Figure S1b, the diffraction peaks at 29.8°, 47.6°, and 52.1° correspond to the (311), (511), and (440) crystal planes of Co<sub>9</sub>S<sub>8</sub> (JCPDS No. 86-2273), respectively.<sup>[4b]</sup> In addition, the characteristic peaks of hexagonal ZnIn<sub>2</sub>S<sub>4</sub> (JCPDS No. 65-2023) are observed at 21.6°, 27.7°, 47.2°, 52.4°, and 55.6°, which are well indexed to the (006), (102), (110), (116), and (022) planes, respectively (Figure S1c).<sup>[3a, 5a]</sup> As expected, the prepared heterostructures display both characteristic peaks of Co<sub>9</sub>S<sub>8</sub> and ZnIn<sub>2</sub>S<sub>4</sub>, and no impurity peaks are observed, suggesting that they are two-phase composites. Moreover, it should be noted that the intensity of the (311) diffraction peak gradually increases with increasing Co<sub>9</sub>S<sub>8</sub> content, together with a decrease of the (110) peak intensity of ZnIn<sub>2</sub>S<sub>4</sub> (Figure 3a). Especially for 20%-Co<sub>9</sub>S<sub>8</sub>/ZnIn<sub>2</sub>S<sub>4</sub>, it can be clearly observed that the diffraction peaks in the XRD patterns (Figure S1d) correspond to those of Co<sub>9</sub>S<sub>8</sub> and ZnIn<sub>2</sub>S<sub>4</sub> standard patterns, confirming that Co<sub>9</sub>S<sub>8</sub>/ZnIn<sub>2</sub>S<sub>4</sub> heterostructures were successfully prepared with a highly crystalline structure.

In-depth investigation of the elemental composition and surface chemical states of the Co<sub>9</sub>S<sub>8</sub>/ZnIn<sub>2</sub>S<sub>4</sub> composite using X-ray photoelectron spectroscopy (XPS) characterization was then performed. The XPS survey spectrum (Figure S7) reveals the

existence of Zn, In, Co, and S elements in the composite. In Figure S8a, the two peaks with binding energies of 1044.5 and 1021.5 eV were assigned to Zn 2p<sub>1/2</sub> and Zn 2p<sub>3/2</sub>, respectively, indicating the Zn(II) oxidation state of ZnIn<sub>2</sub>S<sub>4</sub>.<sup>[13]</sup> In addition, the In 3d high-resolution XPS spectrum (Figure S8b) shows two peaks at 444.9 eV (In 3d<sub>5/2</sub>) and 452.5 eV (In 3d<sub>3/2</sub>), indicating that the chemical state of the In cation in the composite was +3.<sup>[11b]</sup> The Co 2p spectrum in Figure 3b consists of two spin-orbit doublets and two satellite peaks (identified as “Sat.”). The first doublet peaks at 778.5 and 781.1 eV and the second doublet peaks at 793.4 and 797.3 eV correspond to Co 2p<sub>3/2</sub> and Co 2p<sub>1/2</sub>, respectively. The doublets indicate the co-existence of Co<sup>2+</sup> and Co<sup>3+</sup>, which is consistent with previous work.<sup>[9]</sup> Moreover, compared with that of pure Co<sub>9</sub>S<sub>8</sub>, the binding energies of Co 2p shifted from 778.1 and 793.7 eV in Co<sub>9</sub>S<sub>8</sub> to 778.5 and 793.4 eV in the Co<sub>9</sub>S<sub>8</sub>/ZnIn<sub>2</sub>S<sub>4</sub> composite, suggesting a strong interface interaction between Co<sub>9</sub>S<sub>8</sub> and ZnIn<sub>2</sub>S<sub>4</sub>.<sup>[4b, 6, 8b]</sup> In the high-resolution XPS spectrum of S 2p (Figure 3c), the peaks at binding energies of approximately 163.8 and 162.3 eV correspond to the S 2p<sub>1/2</sub> and S 2p<sub>3/2</sub> orbitals of S<sup>2-</sup> ions, which is consistent with the formation of ZnIn<sub>2</sub>S<sub>4</sub>. The other two S 2p peaks at 163.1 and 161.6 eV are attributed to the S 2p<sub>1/2</sub> and S 2p<sub>3/2</sub> orbitals of Co–S bondings, consistent with the results of previous reports on Co<sub>9</sub>S<sub>8</sub>.<sup>[4b, 7, 8b]</sup> Therefore, the XPS spectra of Co 2p and S 2p combined with the XRD results further confirm the existence of Co<sub>9</sub>S<sub>8</sub>. The XPS results also confirm that the prepared composites contained Co<sub>9</sub>S<sub>8</sub> and ZnIn<sub>2</sub>S<sub>4</sub> without any other impurities.

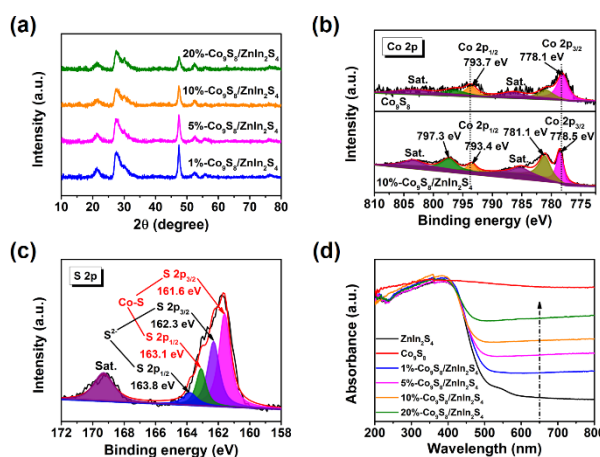


**Figure 3.** (a) XRD patterns of the as-prepared Co<sub>9</sub>S<sub>8</sub>/ZnIn<sub>2</sub>S<sub>4</sub> composites. (b–c) High-resolution XPS spectra of Co 2p and S 2p regions of 10%-Co<sub>9</sub>S<sub>8</sub>/ZnIn<sub>2</sub>S<sub>4</sub> composite. (d) UV–vis diffuse reflectance spectra of the as-prepared Co<sub>9</sub>S<sub>8</sub>, ZnIn<sub>2</sub>S<sub>4</sub>, and Co<sub>9</sub>S<sub>8</sub>/ZnIn<sub>2</sub>S<sub>4</sub> composites.

UV–vis diffuse reflectance spectra (DRS) were used to investigate the optical absorption properties and deduce the band gaps of the as-prepared samples. As observed in Figure 3d, pure ZnIn<sub>2</sub>S<sub>4</sub> exhibits an absorption edge at approximately 520 nm, which is consistent with previous reported works. The pristine Co<sub>9</sub>S<sub>8</sub> showed a very broad absorption edge from 300 to 800 nm, indicating that it possesses strong light harvesting in

both the UV and visible regions. All the  $\text{Co}_9\text{S}_8/\text{ZnIn}_2\text{S}_4$  composites manifested a similar absorption edge in shape. In addition, compared with that of  $\text{ZnIn}_2\text{S}_4$ , the absorption intensities of the  $\text{Co}_9\text{S}_8/\text{ZnIn}_2\text{S}_4$  composites in the visible light region increased with increasing  $\text{Co}_9\text{S}_8$  content, which is consistent with the color of the as-prepared samples changing from light yellow to dark gray (Figure S9).<sup>[14]</sup> The band gap values ( $E_g$ ) of  $\text{ZnIn}_2\text{S}_4$  and  $\text{Co}_9\text{S}_8$  were calculated to be 2.44 and 1.32 eV, respectively, according to the Tauc plot shown in Figure S10. Furthermore, Mott-Schottky plots (M-S) were constructed to define the types of conductivity and the derived flat band potential for semiconductors. As displayed in Figure S11a and b, both  $\text{ZnIn}_2\text{S}_4$  and  $\text{Co}_9\text{S}_8$  exhibited typical characteristics of n-type semiconductors because of the positive slope of the M-S plots. The derived flat-band potentials ( $V_{fb}$ ) of  $\text{ZnIn}_2\text{S}_4$  and  $\text{Co}_9\text{S}_8$  are about -0.92 and -0.66 V versus Ag/AgCl (pH=6.8), respectively. Therefore, the  $V_{fb}$  of  $\text{ZnIn}_2\text{S}_4$  and  $\text{Co}_9\text{S}_8$  were calculated to be -0.72 and -0.46 V versus the normal hydrogen electrode (NHE), respectively. It is well known that the value of the flat band potential roughly equals that of the conduction band potential ( $E_{CB}$ ) for n-type semiconductors.<sup>[11c, 15]</sup> Therefore, the conduction band potential of  $\text{ZnIn}_2\text{S}_4$  and  $\text{Co}_9\text{S}_8$  are -0.72 and -0.46 V, respectively. Using the formula  $E_g = E_{VB} - E_{CB}$ , the valence band potential ( $E_{VB}$ ) of  $\text{ZnIn}_2\text{S}_4$  and  $\text{Co}_9\text{S}_8$  were calculated to be 1.72 and 0.86 V, respectively. Thus, the relevant optical light absorption properties and band structures of the prepared samples were determined.

Cycling tests of photocatalytic reduction of aqueous Cr(VI) by 10%- $\text{Co}_9\text{S}_8/\text{ZnIn}_2\text{S}_4$  composite.

The photocatalytic water splitting was first implemented with triethanolamine (TEOA) as the hole scavenger to examine the photocatalytic performance of the pure  $\text{Co}_9\text{S}_8$ ,  $\text{ZnIn}_2\text{S}_4$ , and  $\text{Co}_9\text{S}_8/\text{ZnIn}_2\text{S}_4$  composites under visible-light irradiation. Figure 4a summarizes the  $\text{H}_2$  evolution amount of pure  $\text{Co}_9\text{S}_8$  and  $\text{ZnIn}_2\text{S}_4$  and different ratios of  $\text{Co}_9\text{S}_8/\text{ZnIn}_2\text{S}_4$  composites within 5 h. The amount of  $\text{H}_2$  generated from samples steadily increased over time. The corresponding photocatalytic  $\text{H}_2$  evolution rates of these samples are also shown in Figure 4b. The pure  $\text{Co}_9\text{S}_8$  displayed negligible photocatalytic activity for  $\text{H}_2$  evolution ( $9 \mu\text{mol h}^{-1} \text{g}^{-1}$ ), most likely because of the high recombination rate of photogenerated electrons and holes.<sup>[9]</sup> The nanosheet-assembled  $\text{ZnIn}_2\text{S}_4$  spheres are active to photocatalytic water splitting with the  $\text{H}_2$ -evolution rate of  $804 \mu\text{mol h}^{-1} \text{g}^{-1}$ . In contrast, all the hierarchical  $\text{Co}_9\text{S}_8/\text{ZnIn}_2\text{S}_4$  tubular heterostructures demonstrated substantially improved rates of  $\text{H}_2$  evolution after growing  $\text{ZnIn}_2\text{S}_4$  nanosheets on the hollow  $\text{Co}_9\text{S}_8$  nanotubes. In addition, it should be noted that the  $\text{H}_2$  evolution rate gradually increases as the  $\text{Co}_9\text{S}_8$  content increased from 1% to 10%. However, a decreased  $\text{H}_2$  evolution rate can be observed when the  $\text{Co}_9\text{S}_8$  content in the composite was further increased to 20%. The optimal  $\text{Co}_9\text{S}_8/\text{ZnIn}_2\text{S}_4$  composites exhibited the highest  $\text{H}_2$ -evolution rate of  $9039 \mu\text{mol h}^{-1} \text{g}^{-1}$  without the use of any co-catalysts (metal complex, noble metal, etc.), which is approximately 11.2 times higher than that of pure  $\text{ZnIn}_2\text{S}_4$ . For comparison, the physical mixture of  $\text{Co}_9\text{S}_8$  (10 wt%) and  $\text{ZnIn}_2\text{S}_4$  (denoted as PM-( $\text{Co}_9\text{S}_8+\text{ZnIn}_2\text{S}_4$ )) was also investigated for photocatalytic  $\text{H}_2$  evolution under the same condition (Figure S12). Obviously, the hierarchical core-shell 10%- $\text{Co}_9\text{S}_8/\text{ZnIn}_2\text{S}_4$  composite demonstrated considerably enhanced  $\text{H}_2$  evolution activity. It suggests that the strong coupling effect between  $\text{Co}_9\text{S}_8$  nanotubes and  $\text{ZnIn}_2\text{S}_4$  nanosheets is extremely beneficial for the photogenerated charge transfer. Moreover, we observed that the wavelength-dependent hydrogen evolution efficiency was well agreement with the light absorption capacity of  $\text{ZnIn}_2\text{S}_4$ , not with that of 10%- $\text{Co}_9\text{S}_8/\text{ZnIn}_2\text{S}_4$  composite (Figure 4c), it can be deduced that the photogenerated electrons come from the  $\text{ZnIn}_2\text{S}_4$ , and  $\text{Co}_9\text{S}_8$  consume the electrons to catalyze the evolution of  $\text{H}_2$ .<sup>[16]</sup> At the same time, the 10%- $\text{Co}_9\text{S}_8/\text{ZnIn}_2\text{S}_4$  composite in this study has a peak external quantum efficiency (EQE) of 4.49% at 420 nm and 0.007% at 550 nm (Table S2), suggesting the well photocatalytic activities in the wavelength range of 550 nm.<sup>[17]</sup> The as-prepared hierarchical hollow  $\text{Co}_9\text{S}_8/\text{ZnIn}_2\text{S}_4$  tubular heterostructures display satisfactory noble-metal-free  $\text{H}_2$  generation rate and EQE relative to that reported in recent works (Table S1). The photocatalytic performance of water splitting was enhanced by the unique hierarchical hollow tubular heterostructures, which can promote the separation and transfer efficiency of photogenerated electrons and holes. The photostability of the optimal  $\text{Co}_9\text{S}_8/\text{ZnIn}_2\text{S}_4$  composite was evaluated through the photocatalytic  $\text{H}_2$  evolution reaction in the

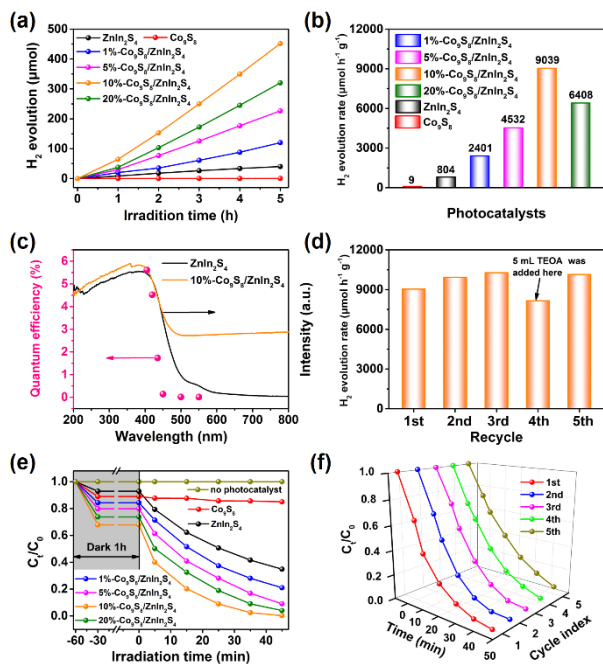


**Figure 4.** (a) Amounts of  $\text{H}_2$  generated from the prepared  $\text{Co}_9\text{S}_8$ ,  $\text{ZnIn}_2\text{S}_4$ , and  $\text{Co}_9\text{S}_8/\text{ZnIn}_2\text{S}_4$  composites in 5 h under visible-light irradiation. (b) Apparent photocatalytic  $\text{H}_2$  evolution rates over the prepared samples. (c) Wavelength dependence of quantum hydrogen evolution efficiency of 10%- $\text{Co}_9\text{S}_8/\text{ZnIn}_2\text{S}_4$  composite. (d)  $\text{H}_2$  generation rate in every 5-h reaction for successive five cycles by 10%- $\text{Co}_9\text{S}_8/\text{ZnIn}_2\text{S}_4$  composite. (e) Photocatalytic reduction of aqueous Cr(VI) by as-prepared samples under visible-light irradiation. (f)

presence of a prolonged visible-light irradiation of 25 h, and the  $H_2$  evolution rate for every 5-h reaction was calculated (**Figure 4d**). In addition, the sacrificial agent (TEOA) was rapidly consumed through oxidation by holes in the photocatalytic  $H_2$  evolution reaction because of the high  $H_2$  evolution rate.<sup>[18]</sup> Therefore, the  $H_2$  evolution rate slightly decreased after three cycles. However, the photocatalytic  $H_2$  evolution rate was recovered when an additional 5 mL of TEOA was added to the reaction system, indicating that the prepared  $Co_9S_8/ZnIn_2S_4$  heterostructures in this study possess good stability for  $H_2$  evolution. The subsequent XRD and TEM measurements after the cycles further confirmed this finding. The XRD pattern of the recycled photocatalyst, named 10%- $Co_9S_8/ZnIn_2S_4$ -AP, was consistent with that of the initial sample, and the positions of the characteristic peaks did not obviously shift (**Figure S13a**). Additionally, the composite after the photocatalytic cycling tests still maintained a hierarchical hollow core-shell tubular configuration (**Figure S13b**).

Then, we evaluated the photocatalytic performance of the as-prepared samples through photocatalytic reduction of aqueous Cr(VI) under visible-light irradiation. Based on our reported works, the standard diphenylcarbazide (DPC) method and UV-vis spectroscopy were used synergistically to monitor the temporal change of the Cr(VI) concentration during the catalytic reactions (**Figure S14**).<sup>[5b]</sup> Before illumination, the prepared photocatalysts and aqueous Cr(VI) solution were mixed and stirred for 1 h under dark conditions to reach the adsorption-desorption equilibrium. As depicted in **Figure 4e**, without the addition of photocatalysts, the concentration of Cr(VI) did not change and remained stable under long-term visible-light irradiation, suggesting that the preparation of catalysts in this study plays an essential role in the photocatalytic reduction of Cr(VI). In addition, all of the  $Co_9S_8/ZnIn_2S_4$  composites exhibited higher adsorption properties for Cr(VI), which contributed to the contact of the photocatalyst with Cr(VI) molecules and accelerated the subsequent photocatalytic Cr(VI) reduction reactions. In the photocatalytic part, the photocatalytic activities of the  $Co_9S_8/ZnIn_2S_4$  composites for the reduction of Cr(VI) were significantly higher than those of pure  $Co_9S_8$  and  $ZnIn_2S_4$ . This enhanced photocatalytic activity mainly resulted from  $Co_9S_8$  and  $ZnIn_2S_4$  having unique hierarchical hollow heterostructures and effectively promoting the interfacial separation and transfer of photogenerated electrons ( $e^-$ ) and holes ( $h^+$ ).<sup>[4b, 5c, 11c]</sup> Moreover, the 10%- $Co_9S_8/ZnIn_2S_4$  composite exhibited the highest photocatalytic activity, and the corresponding reduction efficiency of Cr(VI) reached 100% under 45-min visible-light irradiation. The high-resolution Cr 2p spectrum of the 10%- $Co_9S_8/ZnIn_2S_4$  composite after the photocatalytic reaction is shown in **Figure S15**. The binding energy peak of Cr 2p<sub>3/2</sub> is 577.2 eV, which is consistent with Cr(III) in  $Cr(OH)_3$ .<sup>[5b]</sup> Simultaneously, the photocatalytic reduction kinetic curves of Cr(VI) over the as-prepared samples and relevant apparent reaction rate constants ( $k$ ) are presented in **Figure S16a** and **b**. All the kinetic curves appear as straight lines, indicating that

photocatalytic reduction of Cr(VI) is consistent with a pseudo-first-order model. After introducing  $Co_9S_8$  into  $ZnIn_2S_4$ , the optimized  $Co_9S_8/ZnIn_2S_4$  composite exhibited the highest reaction rate constant, which was 3.98 times higher than that of pure  $ZnIn_2S_4$ . Simultaneously, the photocatalytic performance of PM- $(Co_9S_8+ZnIn_2S_4)$  was clearly lower than that of 10%- $Co_9S_8/ZnIn_2S_4$  composite in the photocatalytic Cr(VI) reduction reactions, indicating that the heterostructural effect was responsible for promoting electron transfer and separation (**Figure S17**). Besides, the results of ESR and scavenger tests revealed that both electrons ( $e^-$ ) and superoxide radicals ( $\cdot O_2^-$ ) were responsible for photocatalytic reduction of Cr(VI) in this study (**Figure S18**), whereas  $e^-$  predominated the photocatalytic reduction of Cr(VI) and  $\cdot O_2^-$  played only a relatively minor role in the case of using as 10%- $Co_9S_8/ZnIn_2S_4$  photocatalyst.<sup>[5b, 19, 20-21]</sup> Finally, we also conducted recycling tests of photocatalytic Cr(VI) reduction to observe the stability of the  $Co_9S_8/ZnIn_2S_4$  photocatalysts. As displayed in **Figure 4f**, the photocatalytic reduction efficiency of Cr(VI) remained high (92.77%) after five cycling runs, suggesting that the prepared  $Co_9S_8/ZnIn_2S_4$  heterostructures has good stability for Cr(VI) reduction. Therefore, the above photocatalytic results indicate that the  $Co_9S_8/ZnIn_2S_4$  composites are capable of effectively water splitting and reducing Cr(VI) to Cr(III), and exhibit good stability under visible light irradiation.

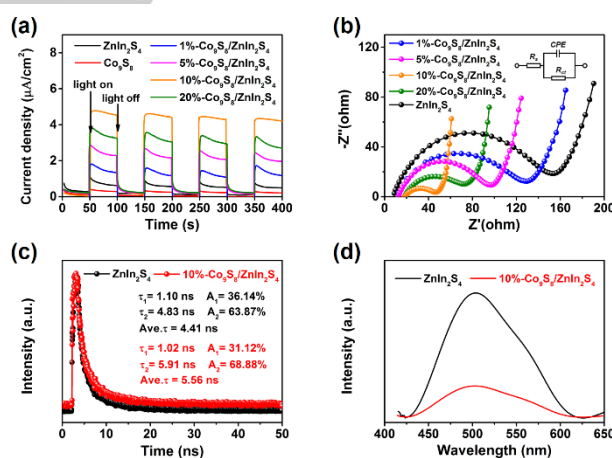


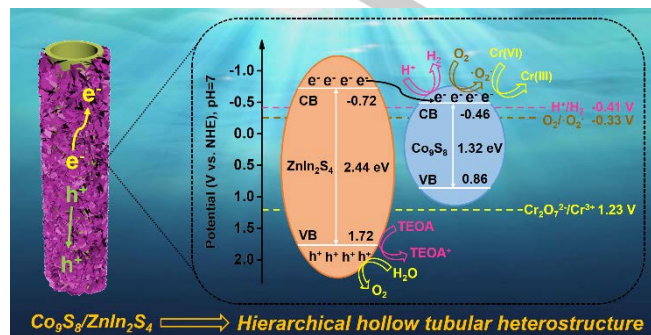
**Figure 5.** (a-b) Photocurrent responses and EIS spectra of as-prepared samples under visible-light irradiation (insert: the corresponding equivalent circuit). (c-d) Time-resolved transient PL decay and steady-state PL spectra of as-prepared  $ZnIn_2S_4$  and 10%- $Co_9S_8/ZnIn_2S_4$  composite.

To investigate the separation-recombination efficiency of photogenerated charge of these  $Co_9S_8/ZnIn_2S_4$  composites, common photo/electrochemical characterizations were performed in this work. As illustrated in **Figure 5a**, all of the prepared photocatalysts exhibited reproducible photocurrent responses for each illumination period, and the photocurrent dropped rapidly in the dark during four on-off cycles of light irradiation. In addition, all of the  $Co_9S_8/ZnIn_2S_4$  composites exhibited better photocurrent responses than those of pure  $Co_9S_8$  and  $ZnIn_2S_4$  catalysts, and the 10%- $Co_9S_8/ZnIn_2S_4$

composite displayed the highest photocurrent responses under visible light. This finding demonstrates that these  $\text{Co}_9\text{S}_8/\text{ZnIn}_2\text{S}_4$  composites possess excellent separation efficiency of electrons ( $e^-$ ) and holes ( $h^+$ ). Electrochemical impedance spectroscopy (EIS) measurements showed that the  $\text{Co}_9\text{S}_8/\text{ZnIn}_2\text{S}_4$  composites had a smaller semicircle than pure  $\text{ZnIn}_2\text{S}_4$  after introducing  $\text{Co}_9\text{S}_8$  co-catalyst, confirming the faster electron transfer in the composites (**Figure 5b and S19**). Simultaneously, time-resolved photoluminescence (PL) spectroscopy was performed to study the charge-carrier dynamics of the materials. As observed in **Figure 5c**, the average emission lifetime of 10%- $\text{Co}_9\text{S}_8/\text{ZnIn}_2\text{S}_4$  composite (5.56 ns) is longer than that of  $\text{ZnIn}_2\text{S}_4$  (4.41 ns). In addition, the steady-state PL spectra (**Figure 5d**) reveal that the 10%- $\text{Co}_9\text{S}_8/\text{ZnIn}_2\text{S}_4$  composite had a lower PL intensity than pure  $\text{ZnIn}_2\text{S}_4$ . These PL results indicate that the recombination of electrons and holes is effectively suppressed in the  $\text{Co}_9\text{S}_8/\text{ZnIn}_2\text{S}_4$  composite. In summary, these photo/electrochemical measurements suggest that the construction of a hierarchical hollow  $\text{Co}_9\text{S}_8/\text{ZnIn}_2\text{S}_4$  heterostructure can accelerate the separation and migration efficiency of photogenerated electrons and holes, which are highly favorable for photocatalytic  $\text{H}_2$  evolution and Cr(VI) reduction reactions in this study.

Based on the characterization analyses and photocatalytic experimental results in this study, the possible charge-transfer process and relevant photocatalytic mechanism of the  $\text{Co}_9\text{S}_8/\text{ZnIn}_2\text{S}_4$  heterostructure in  $\text{H}_2$  evolution and Cr(VI) reduction reactions are discussed in **Scheme 2**. First, when the co-catalyst  $\text{Co}_9\text{S}_8$  nanotubes are covered with  $\text{ZnIn}_2\text{S}_4$  nanosheets, a type-I heterostructure is constructed because of their matched conduction band (CB) and valence band (VB) potentials. Then,  $\text{ZnIn}_2\text{S}_4$  nanosheets are excited to generate electrons ( $e^-$ ) and holes ( $h^+$ ) after the  $\text{Co}_9\text{S}_8/\text{ZnIn}_2\text{S}_4$  composite is illuminated by visible light. Meanwhile, because of the configuration of a heterostructure between  $\text{ZnIn}_2\text{S}_4$  and  $\text{Co}_9\text{S}_8$ , and the CB potential of  $\text{ZnIn}_2\text{S}_4$  ( $-0.72$  V vs. NHE) is more positive than that of co-catalyst  $\text{Co}_9\text{S}_8$  ( $-0.46$  V vs. NHE), therefore the photogenerated electrons from the CB of  $\text{ZnIn}_2\text{S}_4$  can rapidly migrate to that of co-catalyst  $\text{Co}_9\text{S}_8$ . Consequently, the photogenerated electron-hole pairs are effectively separated in the  $\text{Co}_9\text{S}_8/\text{ZnIn}_2\text{S}_4$  heterostructure, and their recombination is dramatically suppressed compared with that of the single components.<sup>[19]</sup> Besides, the open hollow structure of prepared samples allows multiple reflections of light inside the cavity and fast mass transfer, thus accelerating the photocatalytic reactions and achieving higher photocatalytic activity than the solid heterojunction.<sup>[7, 11b]</sup> Finally, in the photocatalytic  $\text{H}_2$  evolution system, the electrons can directly react with  $\text{H}^+$  in water to produce  $\text{H}_2$  ( $-0.41$  V vs. NHE), while the holes are ultimately quenched by the TEOA (sacrificial donor) to an oxidative donor ( $\text{TEOA}^+$ ).<sup>[22]</sup> In the photocatalytic reduction of Cr(VI) reaction, the accumulated electrons can reduce Cr(VI) to Cr(III) (1.23 V vs. NHE) while photogenerated holes oxidize water to  $\text{O}_2$ .<sup>[10, 21]</sup> In addition, the oxygen adsorbed on  $\text{ZnIn}_2\text{S}_4$  can be reduced to

superoxide radicals ( $\cdot\text{O}_2^-$ ) by the electrons from the CB of  $\text{ZnIn}_2\text{S}_4$ , which can accelerate the reduction of Cr(VI).<sup>[3c, 10, 19-21]</sup> Hence, the advantageous combination of light harvesting induced by the open hollow structure and unique hierarchical heterostructure constructed between  $\text{ZnIn}_2\text{S}_4$  nanosheets and  $\text{Co}_9\text{S}_8$  nanotubes can effectively increase the visible-light response for  $\text{H}_2$  evolution and Cr(VI) reduction.



**Scheme 2.** Schematic illustration of the transfer process of the photogenerated electrons ( $e^-$ ) and holes ( $h^+$ ) in the  $\text{Co}_9\text{S}_8/\text{ZnIn}_2\text{S}_4$  heterostructure and the photocatalytic mechanism for Cr(VI) reduction and  $\text{H}_2$  evolution under visible-light irradiation.

## Conclusion

$\text{Co}_9\text{S}_8/\text{ZnIn}_2\text{S}_4$  hierarchical tubular heterostructures were successfully prepared by growing 2D  $\text{ZnIn}_2\text{S}_4$  nanosheets on 1D hollow  $\text{Co}_9\text{S}_8$  nanotubes. The constructed  $\text{Co}_9\text{S}_8/\text{ZnIn}_2\text{S}_4$  hierarchical hollow structures exhibited improved light absorption ability, possessed a large surface area, and exposed rich catalytically reactive sites. Moreover, photo/electrochemical characterization revealed that the introduction of  $\text{Co}_9\text{S}_8$  can significantly enhance the separation and transfer efficiency of photogenerated electrons and holes. As a result, the optimized  $\text{Co}_9\text{S}_8/\text{ZnIn}_2\text{S}_4$  photocatalyst exhibited the highest photocatalytic activity, which can be 100% reduction of Cr(VI) in 45 min. Simultaneously, the optimal  $\text{Co}_9\text{S}_8/\text{ZnIn}_2\text{S}_4$  photocatalyst exhibited a  $\text{H}_2$  evolution rate of  $9039 \mu\text{mol h}^{-1} \text{g}^{-1}$  without the use of any cocatalysts; this rate is 11.2 times higher than that of pure  $\text{ZnIn}_2\text{S}_4$ . In addition, the  $\text{Co}_9\text{S}_8/\text{ZnIn}_2\text{S}_4$  photocatalyst possessed high stability after five photocatalytic cycles under visible-light irradiation. Therefore, we believe that the efficient and stable  $\text{Co}_9\text{S}_8/\text{ZnIn}_2\text{S}_4$  heterostructures prepared in this work are promising photocatalysts for environmental purification and energy conversion applications.

## Acknowledgements

We gratefully acknowledge the financial support provided by the National Key R&D Program of China (2017YFC0210901, 2017YFC0210906), National Natural Science Foundation of China (51573122, 21722607, 21776190), Natural Science Foundation of the Jiangsu Higher Education Institutions of China (17KJA430014, 17KJA150009), the Science and Technology

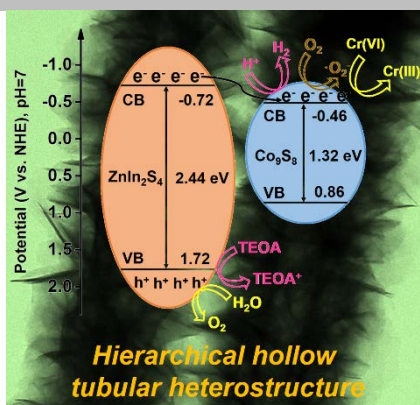
Program for Social Development of Jiangsu (BE2015637) and the project supported by the Priority Academic Program Development of Jiangsu Higher Education Institutions (PAPD). We gratefully acknowledge Dr. Ying Wang, Jing Ye, Xing Zhu, Muzi Chen and Jun Guo from the Testing and Analysis Center of Soochow University for characterizations. We also gratefully acknowledge Dr. Xingwang Zhu, Prof. Hui Xu from Institute for Energy Research of Jiangsu University.

**Keywords:**  $\text{Co}_9\text{S}_8/\text{ZnIn}_2\text{S}_4$  nanotubue • Photocatalysis • Hierarchical heterostructures • Energy conversion • Environmental remediation

- [1] a) J. Hu, D. Chen, Z. Mo, N. Li, Q. Xu, H. Li, J. He, H. Xu, J. Lu, *Angew. Chem.* **2019**, *131*, 2095-2099; b) J. Shen, Y. Li, H. Zhao, K. Pan, X. Li, Y. Qu, G. Wang, D. Wang, *Nano Res.* **2019**, *12*, 1931-1936.
- [2] a) Y. Pu, Y. Luo, X. Wei, J. Sun, L. Li, W. Zou, L. Dong, *Appl. Catal. B* **2019**, *254*, 580-586; b) ST. Kochuveedu, YH. Jang, DH. Kim, *Chem. Soc. Rev.* **2013**, *42*, 8467-8493; c) S. Sun, X. Yu, Q. Yang, Z. Yang, S. Liang, *Nanoscale Adv.* **2019**, *1*, 34-63.
- [3] a) S. Chandrasekaran, L. Yao, L. Deng, C. Bowen, Y. Zhang, S. Chen, Z. Lin, F. Peng, P. Zhang, *Chem. Soc. Rev.* **2019**, *48*, 4178-4280; b) L. Cheng, Q. Xiang, Y. Liao, H. Zhang, *Energy Environ. Sci.* **2018**, *11*, 1362-1391; c) L. Jing, Y. Xu, M. Xie, J. Liu, J. Deng, L. Huang, H. Xu, H. Li, *Chem. Eng. J.* **2019**, *360*, 1601-1612; d) M. Liu, Y. Chen, J. Su, J. Shi, X. Wang, L. Guo, *Nat. Energy* **2016**, *1*, 16151; e) J. Zhang, J. Yu, Y. Zhang, Q. Li, J. Gong, *Nano Lett.* **2011**, *11*, 4774-4779.
- [4] a) H. Liu, J. Zhang, D. Ao, *Appl. Catal. B* **2018**, *221*, 433-442; b) S. Wang, B. Guan, X. Wang, X. Lou, *J. Am. Chem. Soc.* **2018**, *140*, 15145-15148.
- [5] a) W. Li, Z. Lin, G. Yang, *Nanoscale* **2017**, *9*, 18290-18298; b) G. Zhang, D. Chen, N. Li, Q. Xu, H. Li, J. He, J. Lu, *Appl. Catal. B* **2018**, *232*, 164-174; c) S. Wang, B. Guan, X. Lou, *J. Am. Chem. Soc.* **2018**, *140*, 5037-5040.
- [6] S. Wang, Y. Wang, S. Zhang, S. Zhang, X. Lou, *Adv. Mater.* **2019**, *31*, 1903404.
- [7] B. Qiu, Q. Zhu, M. Du, L. Fan, M. Xing, J. Zhang, *Angew. Chem. Int. Ed.* **2017**, *56*, 2684-2688.
- [8] a) S. Deng, Y. Zhong, Y. Zeng, Y. Wang, X. Wang, X. Lu, X. Xia, J. Tu, *Adv. Sci.* **2018**, *5*, 1700772; b) H. Zhu, J. Zhang, R. Yanzhang, M. Du, Q. Wang, G. Gao, J. Wu, G. Wu, M. Zhang, B. Liu, J. Yao, X. Zhang, *Adv. Mater.* **2015**, *27*, 4752-4759.
- [9] P. Tan, Y. Liu, A. Zhu, W. Zeng, H. Cui, J. Pan, *ACS Sustainable Chem. Eng.* **2018**, *6*, 10385-10394.
- [10] J. Gua, H. Chen, F. Jiang, X. Wang, L. Li, *Chem. Eng. J.* **2019**, *360*, 1188-1198.
- [11] a) S. Wang, Y. Wang, S. Zhang, X. Lou, *Small Methods* **2019**, 1900586; b) P. Zhang, X. Lou, *Adv. Mater.* **2019**, *31*, 1900281; c) S. Wang, B. Guan, Y. Lu, X. Lou, *J. Am. Chem. Soc.* **2017**, *139*, 17305-17308; d) S. Wang, B. Guan, X. Lou, *Energy Environ. Sci.* **2018**, *11*, 306-310.
- [12] H. Yuan, Q. Jiao, J. Liu, X. Liu, H. Yang, Y. Zhao, Q. Wu, D. Shi, H. Li, *J. Power. Sources* **2016**, *336*, 132-142.
- [13] M. Yang, Y. Xu, W. Lu, K. Zeng, H. Zhu, Q. Xu, G. Ho, *Nat. Commun.* **2017**, *8*, 14224.
- [14] L. Ye, J. Fu, Z. Xu, R. Yuan, Z. Li, *ACS Appl. Mater. Interfaces* **2014**, *6*, 3483-3490.
- [15] R. Tao, C. Zhao, C. Shao, X. Li, X. Li, J. Zhang, S. Yang, Y. Liu, *Mater. Res. Bull.* **2018**, *104*, 124-133.
- [16] a) J. Yi, H. Li, Y. Gong, X. She, Y. Song, Y. Xu, J. Deng, S. Yuan, H. Xu, H. Li, *Appl. Catal. B* **2019**, *243*, 330-336; b) X. Zhu, J. Yang, X. She, Y. Song, J. Qian, Y. Wang, H. Xu, H. Li, Q. Yan, *J. Mater. Chem. A* **2019**, *7*, 5209-5213.
- [17] H. Yang, R. Cao, P. Sun, J. Yin, S. Zhang, X. Xu, *Appl. Catal. B* **2019**, *256*, 117862.
- [18] H. Xu, X. She, T. Fei, Y. Song, D. Liu, H. Li, X. Yang, J. Yang, H. Li, L. Song, P. Ajayan, J. Wu, *ACS Nano* **2019**, *13*, 11294-11302.
- [19] a) H. Huang, S. Tu, C. Zeng, T. Zhang, AH. Reshak, Y. Zhang, *Angew. Chem. Int. Ed.* **2017**, *56*, 11860-11864; b) F. Chen, H. Huang, L. Ye, T. Zhang, Y. Zhang, X. Han, T. Ma, *Adv. Funct. Mater.* **2018**, *28*, 1804284; c) F. Chen, H. Huang, L. Guo, Y. Zhang, T. Ma, *Angew. Chem. Int. Ed.* **2019**, *58*, 10061-10073; d) H. Yu, J. Li, Y. Zhang, S. Yang, K. Han, F. Dong, T. Ma, H. Huang, *Angew. Chem. Int. Ed.* **2019**, *58*, 3880-3884; e) M. Li, S. Yu, H. Huang, X. Li, Y. Feng, C. Wang, Y. Wang, T. Ma, L. Guo, Y. Zhang, *Angew. Chem. Int. Ed.* **2019**, *58*, 9517-9521.
- [20] F. Zhang, Y. Zhang, G. Zhang, Z. Yang, D. D. Dionysiou, A. Zhu, *Appl. Catal. B* **2018**, *236*, 53-63;
- [21] D. Wang, Y. Xu, L. Jing, M. Xie, Y. Song, H. Xu, H. Li, J. Xie, *J. Hazard. Mater.* **2020**, *384*, 121480;
- [22] K. Maeda, *ACS Catal.* **2013**, *3*, 1486-1503.

## RESEARCH ARTICLE

The visible-light-responsive hierarchical  $\text{Co}_9\text{S}_8/\text{ZnIn}_2\text{S}_4$  tubular heterostructures are fabricated by growing two-dimensional  $\text{ZnIn}_2\text{S}_4$  nanosheets on one-dimensional hollow  $\text{Co}_9\text{S}_8$  nanotubes. Meanwhile, the prepared  $\text{Co}_9\text{S}_8/\text{ZnIn}_2\text{S}_4$  heterostructure provides a remarkable  $\text{H}_2$  generation rate of  $9039 \mu\text{mol h}^{-1} \text{g}^{-1}$  without the use of co-catalysts (metal complex, noble metal, etc.), and  $\text{Cr(VI)}$  is completely reduced in 45 min.



Guping Zhang, Dongyun Chen, Najun Li, Qingfeng Xu, Hua Li, Jinghui He, and Jianmei Lu\*

Page No. – Page No.

**Construction of Hierarchical Hollow  $\text{Co}_9\text{S}_8/\text{ZnIn}_2\text{S}_4$  Tubular Heterostructures for Highly Efficient Solar Energy Conversion and Environmental Remediation**